JOURNAL OF PROPULSION AND POWER
Vol. 23, No. 1, January–February 2007

Experimental Characterization of an Isothermal Swirler Flowfield

Mark A. Woodmansee*
General Electric Optimization and Control, Minden, Nevada 89423
Irven C. Ball†
General Electric Aircraft Engines, Lynn, Massachusetts 01910
and
Kenneth W. Barlow‡
Naval Air Systems Command, Patuxent River, Maryland 20670-1534

DOI: 10.2514/1.19105

A method for characterizing the flowfield associated with an ensemble of production swirl cups before their implementation into an aircraft engine is presented. LDV is used to acquire mean, rms, and skewness velocity profiles downstream of the swirlers' venturi. The skewness of the streamwise velocity data is used to locate the fluid boundary between the primary and secondary corotating streams. The data reduction technique utilizes the modality transformation of the streamwise velocity histograms as the LDV probe volume is translated from the low-speed secondary stream to the high-speed primary stream. By locating this boundary, primary and secondary flowfield metrics such as swirl number and primary-secondary mass flow split compliment the conventional effective area measurements. To corroborate the LDV measurements, digital particle image velocimetry images are used to qualify the size and position of the recirculation zone created at the venturi exit as well as highlight the unsteady nature of the feature. Instantaneous side- and end-view digital particle image velocimetry images provide evidence of coherent radial movement, that is, wagging of the recirculation zone and the presence of large-scale vortices in the secondary stream.

Introduction

THE operability limits of an aircraft engine are strongly dependent on the ability of the combustor swirler to stabilize the pilot and main fuel reaction zone within the annular combustor. As one would expect, the airflow pattern through the swirler, often referred to as the "swirl cup," directly affects engine performance parameters [1–4] such as the fuel/air turndown ratio, relight capability at altitude, unburned hydrocarbon (UHC) emissions, and parasitic pressure losses through the combustor. Most common swirler designs employ axial or radial swirl vanes surrounding the fuel injector tip to impart a component of azimuthal velocity (i.e., swirl) to the incoming air. If designed correctly, this bulk fluid rotation generates a central toroidal recirculation zone (CTRZ) by creating an adverse pressure gradient at the center of the swirl cup. Flow within this region follows a toroidal pattern, creating forward and aft stagnation points along the swirler centerline. By creating a recirculation zone in the region where the pilot and main fuel sprays are injected, the breakdown of the nascent fuel droplets is accelerated, further preparing the atomized fuel for combustion. Equally important, the shear layer formed on the boundary of this recirculation zone preheats the incoming air by mixing a portion of the postcombustion products with the relatively cold compressor discharge air that enters the combustor through its head end.

In practice, engine manufacturers typically perform single swirl-cup experiments (e.g., one or two fuel nozzle and swirler assemblies in a sector mock-up of the combustor annulus). These reacting experiments are conducted in a high-pressure combustion facility to evaluate a particular swirler design over a range of engine operating conditions. Unfortunately, these experiments confound the performance of the swirler and fuel nozzle by coupling the gas and liquid phases of the flowfield. For example, poor fuel nozzle performance directly affects the ignition and stabilization characteristics of the combustor reaction zone, regardless of the swirler behavior. Equally important, these experiments tend to be prohibitively expensive and time consuming for large numbers of swirl cup designs.

Using laser Doppler velocimetry (LDV) data, a novel approach to characterize the swirlers' isothermal performance, independent of the fuel nozzle, is presented here. Coupled with conventional effective area experiments [2] these nonintrusive flowfield measurements assist in the quantification of swirler metrics such as swirl number, primary–secondary air mass flow split, recirculation strength, and turbulent kinetic energy (TKE) distribution independent of the fuel injector's performance. This being said, we readily acknowledge that the reacting swirler flowfield differs from the isothermal field. For interested readers, Gupta et al. [5] details the phenomenological differences between reacting and nonreacting swirler flowfields. However, from a manufacturing viewpoint, it is not feasible or financially viable to examine each production swirler under reacting conditions before implementing the examined components into an engine. Instead, we benchmark each component under isothermal conditions, using the skewness from the LDV measurements to identify the time-averaged boundary between the primary and secondary swirler streams, and subsequently the primary mass flow split. These data show that subtle differences in swirler manufacturing processes are identified without having to perform reacting measurements.

Background

Swirl flows [6–15], because of their applicability to land- and air-based gas turbine combustor design, have been studied extensively for more than 40 years [16]. This effort is intended to complement the aforementioned studies by utilizing LDV and digital particle image

Presented as Paper 2864 at the 32nd AIAA Fluid Dynamics Conference and Exhibit, St. Louis, Missouri, 24–26 June 2002; received 25 July 2005; revision received 19 March 2006; accepted for publication 20 March 2006.

*Mechanical Engineer, 1631 Bently Parkway South; mark.woodmansee@ge.com. Senior Member AIAA.
†Mechanical Engineer, 1000 Western Avenue.
‡Aerospace Engineer, 22195 Elmer Road, Building 106.

velocimetry (DPIV) to evaluate the near-field flow of real (1× scale) production aircraft engine swirlers as a standard evaluation process, complementing conventional effective area measurements [2] commonly employed by the gas-turbine industry. The aforementioned laser-based techniques provide spatially resolved data that allow characteristic swirler parameters such as primary mass flow split and swirl number to be calculated for components manufactured with alternative processes or that are different in design.

Effective area measurements are commonly used to demarcate the performance of combustor swirl cups in a cold-flow chamber (i.e., isothermal at ambient temperatures and pressures). The effective areas (primary, secondary, total) of each swirler are acquired over a range of dome pressure drops, $\Delta P/P$, to elucidate the Reynolds-number dependence on the discharge coefficient, C_d. By comparing the effective areas of each swirler, one can differentiate between *gross* component defects and/or obvious design errors before the swirler is implemented into the combustor annulus. Unfortunately these isothermal experiments do not directly address the flowfield nuances imparted by the swirlers. Small mechanical differences, such as increased surface roughness (finish), attached metal flashing, or fillet/chamfer variations created during manufacture can have a pronounced impact on the local flowfield, and hence, performance of the swirl cup.

The application of LDV, DPIV, hot wire, and numerous flow visualization techniques to combustor swirl cups, and swirling flows in general is not new. The book by Gupta et al. [5] is a near-comprehensive work detailing swirling flow theory, swirler design, and application at both low and high swirl numbers. To aid in the design process, the authors primarily focus on the downstream flowfield characteristics (i.e., $z/D \gg 1$) of different radial-, axial-, and circumferential-vane swirlers, comparing and contrasting the decay of the bimodal streamwise velocity distributions found in a recirculating flowfield with the monomodal distributions associated with an axisymmetric turbulent jet. A number of semiempirical correlations for U_z, U_r, and U_θ velocity profiles are presented, detailing the flowfield downstream of the primary recirculation zone. At the time of writing, nonintrusive techniques such as LDV had not been applied extensively to swirling flows.

McGuirk and Palma [10,11] examine the flow inside a water model of a gas turbine combustor, a single "can," using LDV to gather the first through fourth statistical moments [17] of the velocity distributions within the Plexiglass chamber. The authors found that the flow through the primary and dilution holes in the simulated liner strongly affect the swirler flow at the head end of the combustor. In this study, we do not emulate the annular combustion liner to minimize the confounding of the near field by these temporally unsteady jets-in-crossflow downstream.

More recently, Weigand et al. [13] and Meier et al. [14] published detailed thermal, chemical, and velocity data using pointwise and planar laser diagnostics acquired in a corotating swirler flowfield with CH_4-air reaction. These detailed data will provide a solid experimental benchmark for comparison with corresponding numerical efforts. The authors focus on a single swirler design operating at three distinct stoichiometries.

Using two-component LDV, Mehta et al. [18] characterized the flowfield of corotating and counter-rotating combustor swirl cups where the primary and secondary radial swirlers turned the flow in consistent and opposite directions, respectively. By fabricating a 3×-scale model of the swirler, velocity data were captured upstream of the swirler exit within the swirler proper. While the authors discuss the U_z, U_r, and U_θ velocity profile differences in the corotating and counter-rotating streams, only a small portion of the discussion is devoted to the near-field interaction between the primary and secondary streams.

In a two part study, Wang et al. [1,19] acquired LDV and phase-Doppler particle anemometry (PDPA) measurements at different locations in the flowfield of a General Electric CFM-56 combustor swirl cup. Similar to Mehta et al. [18], the radial swirler employed counter-rotating primary and secondary swirlers. To further emulate the entrainment of air due to liquid fuel atomization, water was injected (as a surrogate to aviation fuel) through the fuel atomization nozzle. As an aside, care must be taken in using atomized sprays in isothermal flows to gain insight into combustor performance. In most gas turbine combustors that employ liquid fuel atomization, the elevated static temperatures (i.e., $T > 700$ K) from the combustion process greatly accelerate droplet evaporation [3]. The vapor expansion from the phase change dramatically alters the primary air entrainment. Clearly, the augmented evaporation rate at elevated temperatures will change the drop size distribution in the spray.

As mentioned above, the primary objective of this study is to examine the isothermal flowfield of 1×-scale combustor swirl cups. More specifically, the skewness of the LDV velocity data is used to identify the spatial boundary between the primary and secondary corotating streams. In addition, DPIV flowfield images are used as a qualitative check of the LDV measurements. The streamwise and end-view images provide insight into the periodic excursions of the CTRZ from one side of the swirler shroud to the other. This work extends the efforts of the aforementioned researchers by employing the LDV technique in a manufacturing environment to screen and characterize an ensemble of production swirlers *before* their implementation into an aircraft engine combustor.

Equipment and Facilities

Figure 1 is a centerline section view of the aircraft engine swirler and associated fixture used in these experiments. An air plenum (not shown) with a perforated plate conditions and distributes the flow before it passes through the swirler system. A calibrated venturi flow meter (±1% full scale mass flow uncertainty) upstream of the plenum monitors the mass flow rate of the air entering the plenum and then passing through the swirler. Before reaching the plenum, a portion of the air is directed through a fluidized bed seeder where titanium dioxide (TiO_2) powder is entrained. Experimental light microscopy analyses of the powder determined the average agglomerate size to be $d_p = 0.6$ μm with 95% of all agglomerates less than 2.1 μm in diameter.

The swirler face is referenced and sealed to a machined metal surface on the windward side fixture; see Fig. 1. A machined plug is inserted into the fuel nozzle port to emulate the obstruction imposed by the fuel nozzle in the real engine. As the flow approaches the windward side of the swirler, equally spaced contoured axial vanes turn the flow azimuthally. A venturi attached to the trailing edge of the vanes separates the flow into primary and secondary corotating streams, with a flow split of 65 and 35%, respectively. The swirling flow forms a CTRZ downstream of the venturi. A cylindrical quartz tube [45 mm ID (inner diameter), 48 mm OD (outer diameter)] extending downstream of the swirler face mimics the metal swirler shroud used in a typical aircraft engine. This shroud diminishes the cross-stream ventilation from neighboring swirlers within the annular combustion chamber, while partially confining the flow exiting the swirler.

The origin of the LDV coordinate system, denoted by the letter "O" in Fig. 1, is chosen to begin at the trailing edge of the inner

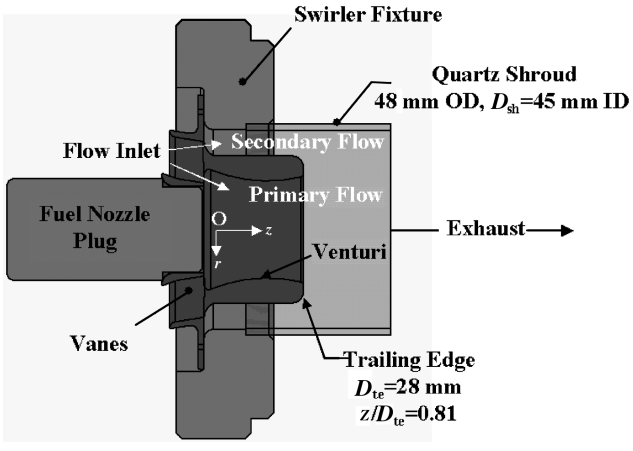

Fig. 1 Schematic of the swirler and associated fixture.

Table 1 LDV system

Parameter	Streamwise	Azimuthal
Channel	1	2
Wavelength	514.5 nm	488.0 nm
Transmitter focal length	500 mm	500 mm
Bragg shift	40 MHz	36 MHz
Fringe spacing	6.43 μm	6.11 μm
Probe volume waist	234 μm	222 μm
Probe volume length	1159 μm	1159 μm

swirler vanes along the centerline of the swirler. The LDV measurements, to be discussed below, are acquired adjacent to the trailing edge of the venturi. An exhaust pipe (not shown in the figure) operating at slightly negative pressure captures the effluent, transporting it outside of the laboratory area. Initial LDV scans were acquired with different exhaust pipe positions to ensure that the limited aspiration of the duct did not influence the local swirler airflow in any manner.

The nonintrusive pointwise velocity measurements are acquired using a two-component fiber-optic LDV system manufactured by Aerometrics, Inc. (Interested readers are referred to Adrian [20] for a detailed description of the theory behind LDV.) Table 1 details the operating characteristics of the LDV system. A receiver placed 12.5 deg off of the forward scattering axis captures the light scattered by the TiO_2 particulate as they pass through the LDV probe volume. Two signal processors (Aerometrics RSA3200-L and RSA3200-P) are used to convert the Mie-scattered light into orthogonal velocity components using digital fast Fourier transform (FFT) algorithms. During the data collection, the particle arrival frequencies ranged from 10 Hz at the cylinder wall to 10 kHz in the swirler freestream. The velocity data are recorded and stored on a Dell OptiPlex GX1 personal computer. Care was taken at the outset of these measurements to ensure that velocity bias [20] effects were in fact negligible. Interested readers are referred to Iyer and Woodmansee [21] for more information regarding the LDV velocity bias studies for this swirling flowfield.

The laser, fiber-optic coupler, LDV transmitter, and receiver reside on a three-dimensional translation stage, allowing the entire system to translate with respect to the stationary swirler plenum. The position uncertainty [21] of the translation stages is ± 0.256 mm. Before each experiment, the probe volume is referenced to the trailing edge of the venturi and then redundantly confirmed with the inner surface of the quartz shroud.

A TSI, Inc. DPIV system is used to capture the two-dimensional velocity fields presented at the end of the Results and Discussion section. The DPIV system employs two New Wave Research Gemini Nd:YAG lasers with a pulse energy and temporal width (full width at half maximum) of 500 mJ and 5 ns, respectively. The frequency-doubled Nd:YAG lasers lase at a wavelength of 532 nm and have a pulse repetition rate of 15 Hz. During operation, the Q-switch timing in the laser oscillator cavities is retarded to provide laser powers less than the aforementioned 500 mJ. After exiting their respective housings, optics are used to combine both beams along a solitary trajectory. A hollow three-bar linkage with 532-nm 100%-reflective mirrors at the end of each appendage directs the laser pulses to an optical head where a laser sheet is formed. To transform the columnar laser pulse into a planar light sheet, the optical head employs a cylindrical lens ($f = -12.7$ mm) followed by a spherical lens ($f = 200$ mm). The relative spacing between these optics is adjusted to create a laser sheet experimentally measured to be 48 mm wide and 60 μm thick.

A single PIVCAM 10-30 630046 CCD camera is used to collect the scattered light from the same TiO_2 particulate as used in the LDV measurements. The 8-bit camera has a 1008×1018 pixel array with a frame-straddling capability, allowing separate flowfield images to be captured and digitized in a period of microseconds. The laser separation delay, controlled by a TSI LaserPulse synchronizer, was set between 6–10 μs depending on the light sheet position and the maximum out-of-plane velocity (as determined by the LDV measurements). Standard TSI Insight (version 3.3) cross-correlation software was used to reduce and spatially filter the raw DPIV images.

Results and Discussion

LDV Results

Table 2 lists the swirler flow conditions. To account for small variations in the ambient environment, the atmospheric pressure, temperature, and relative humidity of the laboratory are recorded before and after each data ensemble is collected. The plenum airflow and stagnation pressure are controlled and monitored with a hand gate valve and water manometer, respectively. Once the flow reaches steady state, LDV measurements are acquired across the swirler exit downstream of the trailing edge of the venturi at $z/D_{te} = 0.88$; see Fig. 1. The trailing edge of the venturi resides at $z/D_{te} = 0.81$. The 514.5 nm and 488.0 nm beams of the LDV system are oriented such that the streamwise and azimuthal velocities, U_z and U_θ, respectively, are captured; the radial velocity (U_r) profiles are not presented here. The LDV measurement spacing is decreased by 50% in regions of high streamwise and azimuthal velocity gradients. At each spatial location, approximately 2000 coincident velocity measurements are captured in each data ensemble. Iyer and Woodmansee [21] determined that 600 realizations are required to gain 95% confidence in the first, second, and third statistical moments in this low-speed swirling flow. To facilitate comparison of the three swirl cups, all LDV and DPIV data presented below have been normalized by the cup-mixing velocity $\bar{U}_z$ exiting the swirler.

Streamwise and azimuthal mean velocity profiles from three swirlers, labeled A, B, and C, are shown in Fig. 2. These swirlers (of identical design) were fabricated by a vendor with the same tool and die and are therefore expected to share similar flow characteristics. In Fig. 2, the plot's abscissa is normalized by the outer diameter of the venturi's trailing edge, D_{te}. The streamwise velocity profile, plotted against the left ordinate in Fig. 2 is qualitatively symmetric about $r/D_{te} = 0$. The two velocity peaks are located slightly inboard ($r/D_{te} = \pm 0.45$) of the venturi outer diameter, suggesting that the primary airflow carries a majority of the streamwise fluid momentum. The central toroidal recirculation zone, where $U_z(r)/\bar{U}_z \leq 0$, occupies approximately 50% of the venturi exit diameter. As one would expect for a CTRZ, the largest negative velocity, $U_z/\bar{U}_z = -1.25$, occurs along the swirler centerline.

The azimuthal velocity $U_\theta(r)/\bar{U}_z$ across the trailing edge of the swirler is plotted against the right ordinate in Fig. 2. The data maintain an asymmetric profile about $r/D_{te} = 0$ due to the counterclockwise rotation of the flow about the swirler centerline. The magnitude of the azimuthal velocity increases in a near-monotonic fashion with radial distance, similar to solid-body rotation [5]. Interestingly, the flow within the core of the recirculation zone, $0.25 < r/D_{te} < 0.25$, does not embody a strong azimuthal component of velocity. This is most likely due to the bluff body imposed by the fuel nozzle plug at the center of the swirler. The swirl number, a measure of the azimuthal momentum flux to the axial momentum flux, is defined as [5]

$$S_N = \frac{G_\theta}{G_x r_o} \tag{1}$$

where

$$G_\theta = \int_{r_i}^{r_o} U_z U_\theta r^2 \mathrm{d}r$$

and

Table 2 Swirler flow parameters

Parameter	Value
Reynolds number	2.6×10^4
Plenum stagnation pressure, gage	4 kPa
Pressure ratio, P_t/P_∞	1.025
Plenum stagnation temperature	304 K

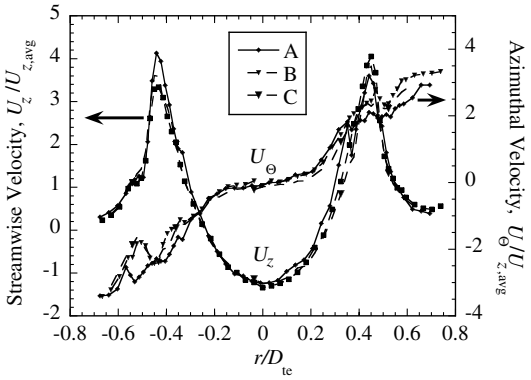

Fig. 2 Mean velocity profiles acquired at $z/D_{te} = 0.88$.

$$G_x = \int_{r_i}^{r_o} U_z^2 r \mathrm{d}r$$

are the angular momentum and axial thrust terms, respectively. The pressure force term, $P - P_\infty$, is neglected in G_x due to the near-atmospheric stagnation pressure within the plenum; see Table 2. More specifically, this thrust term is negligible when compared to the kinetic based terms in Eq. (1). The primary recirculation region boundaries are given by $r_i = 0$ and $r_o = D_{te}/2$. The secondary-flow boundaries are defined as $r_i = D_{te}/2$ and $r_o = D_{sh}/2$ where D_{sh} is the ID of the quartz shroud surrounding the swirl cup shown in Fig. 1.

Using Eq. (1) with the data in Fig. 2, flow within the primary region embodies a swirl number of $S_N \sim 0.55$. Gupta et al. [5] state that S_N must be greater than 0.64 to induce vortex breakdown in a swirling or rotating flowfield. Therefore, this flow would be classified as having a *low* [5] or *moderate* [2] degree of swirl. If this primary stream was simply a free swirling jet propagating into a quiescent environment, the axial adverse pressure gradient in the primary region would not be of sufficient strength to overcome the streamwise momentum of the flow. More succinctly, the flow would not recirculate or form a CTRZ. However, in the swirl cup, the existence of a stronger swirling flow in the secondary stream, where the swirl number is approximately 3 times greater than in the primary stream, provides the required torque (via the interfacial mixing layer) to induce vortex breakdown within the primary flow. The flow within the secondary-flow annulus would be classified as having *high* [5] or *strong* [2] swirl. Comparing the two mean velocity profiles in Fig. 2, it is clear that the elevated swirl number in the secondary region is caused by the precipitous drop in streamwise velocity U_z near the ID of the quartz tube while $|U_\theta|$ reaches a maximum value in this region.

While the streamwise rms profile in Fig. 3a follows a similar trend to the mean velocity profile, the peak rms velocities occur slightly inboard ($r/D_{te} = \pm 0.35$) of the maximum mean streamwise velocities in Fig. 2. Syred and Beér [16] observed that the streamwise fluctuations reach a peak in the viscous mixing region between the counterpropagating fluid within the recirculation zone and the positive streamwise velocity fluid surrounding the CTRZ. As one would expect, the azimuthal rms profile in Fig. 3b is qualitatively symmetric about the centerline. While less clear, the rms distribution is bimodal with peaks at $r/D_{te} \approx \pm 0.25$ and $r/D_{te} \approx \pm 0.46$. Comparing the plots in Figs. 3a and 3b, the radial location of the maximum streamwise rms value essentially bisects the maxima in the azimuthal rms profiles.

Summarizing the results presented in Figs. 2 and 3, the swirling flow within the primary zone ($r/D_{te} = \pm 0.50$) is stochastically unsteady with levels of turbulence intensity ($u_{r,rms}/U_z = 47\%$ and $u_{\theta,rms}/U = 37\%$) that are consistent with low-speed mixing layers. However, unlike a canonical planar two-stream shear layer, the strong azimuthal velocities imparted by the swirler and the presence of the recirculation zone greatly complicate the flowfield. One result of these confounding effects is that none of the streamwise or azimuthal mean and rms peaks are spatially coincident, creating a region of elevated TKE that has a finite radial width.

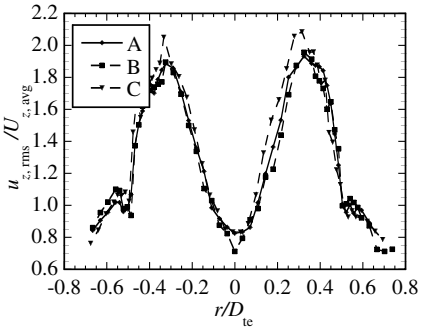

a) Streamwise rms profile

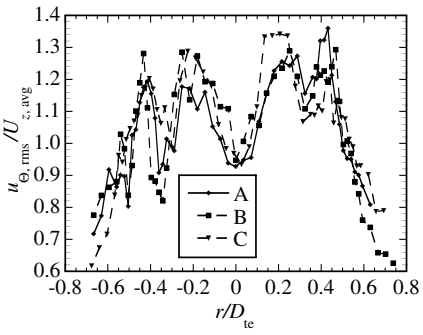

b) Azimuthal rms profile

Fig. 3 rms velocity profiles acquired at $z/D_{te} = 0.88$.

Syred and Beér [16] note that the diverging portion of the swirler nozzle (i.e., venturi) in the primary flow region (see Fig. 1) relaxes the aforementioned $S_N > 0.64$ criterion for the formation of the CTRZ. As for the causality of the secondary stream affecting the behavior of the primary stream, it should be reiterated that the venturi eliminates interaction between the two corotating fluid streams until $z/D_{te} = 0.81$, well downstream of the trailing edge of the axial vanes ($z/D_{te} = 0$). In the combustor, the first opportunity for fluid exchange between reacted and nonreacted species in the primary and secondary streams occurs downstream of the trailing edge of the venturi. However, the forward stagnation point of the CTRZ lies upstream of D_{te}. Moreover, if the curved shape, surface roughness, ovality, or wall thickness of the venturi varies from swirler to swirler, then the primary–secondary stream boundary downstream of this entity will change as well. It will be shown below that the primary mass flow split is sensitive to subtle differences between swirlers.

In general, conventional effective area measurements characterize the pressure loss of the flow as it passes through the swirler system. However, downstream flowfield characteristics, such as the velocity profiles exhibited in Figs. 2 and 3 are not elucidated by this isothermal measurement technique. Likewise, it is not apparent from the mean and rms measurements in Figs. 2 and 3, respectively, where the fluid boundary between the primary and secondary streams resides. As mentioned above, none of the peaks in either the streamwise or azimuthal mean and rms streams are coincident. For example, in Fig. 2, the streamwise velocity decreases in a monotonic manner for $r/D_{te} > \pm 0.45$, while the azimuthal mean velocity profile in Fig. 2 increases linearly until D_{sh} is reached.

One way to quantify or define the beginning of this interfacial boundary between the primary and secondary streams is to use the *skewness* of the LDV data. Skewness [17] S (not to be confused with swirl number, S_N) is a measure of velocity PDF symmetry and shape. This third central moment is defined as

$$S_i = \frac{\sum_1^N (U_i - \bar{U}_i)^3}{(N-1)\sigma_U^3} \tag{2}$$

where U_i and $\bar{U}_i$ are the instantaneous and mean velocities from a directional component i, respectively; N and σ_U are the number of measurement points and standard deviation of the velocity data, respectively. Velocity PDFs with $S < 0$ embody longer "tails" or "wings" that reside at lower velocities; the mean velocity is less than

the median velocity. Similarly, velocity PDFs with $S > 0$ have a longer tail toward the higher velocities and the average velocity is greater than the median value of the data ensemble.

One assumption that must be made in this analysis is that the peak streamwise velocity resides within the primary stream; see Fig. 2. It is conceivable (but not probable) that in a highly three-dimensional flowfield, the secondary stream could embody a strong radially inward velocity at the trailing edge of the venturi such that the peak streamwise velocity at $r/D_{te} = \pm 0.45$ originates from fluid issuing through the secondary vanes. However, the DPIV images presented below show that this scenario is not true. In fact, the peak streamwise velocity emanates from the radially diverging fluid within the primary stream.

Before delving into the experimental data, the analysis technique is first described. For the purpose of explanation only, we assume that the primary and secondary streams embody Gaussian velocity PDFs with the mean streamwise velocities of U_{high} and U_{low}, respectively. As the LDV probe volume is translated radially inward from the quartz shroud toward the swirler centerline, the symmetric monomodal velocity PDF centered about U_{low} with $S_z = 0$ in the secondary freestream will transition to a symmetric monomodal velocity profile centered about U_{high} with $S_z = 0$ in the primary freestream. However, the transition from U_{low} to U_{high} throughout the viscous mixing region is neither instantaneous nor discreet. As the LDV probe volume encounters parcels of higher-velocity fluid from the primary stream, the monomodal U_{low} velocity PDF becomes "skewed" toward higher velocities (i.e., $S_z > 0$). Translating the probe volume further toward the primary stream, the rightmost (higher velocity) tail of the PDF begins to become more populated. Ultimately, the probe volume will straddle the two streams as an equal number of fluid parcels at U_{low} and U_{high} pass through the LDV probe volume. At this point the velocity PDF is bimodal with S_z again equal to zero. This occurs when the two peaks corresponding to U_{low} and U_{high} are present with the left and right wings of the velocity PDF and are nearly equal in height. We define this location as the fluid boundary between the primary and secondary streams. As the probe volume moves further into the primary stream, the velocity PDF is transformed once again into a monomodal profile. However, unlike the monomodal profile in the secondary stream, the velocity PDF now has a maximum at U_{high} with a longer tail at lower velocities ($S_z < 0$).

The experimentally measured streamwise velocity histograms for swirler A are displayed in Figs. 4 and 5, respectively, providing experimental evidence for the above discussion. (Data from swirlers B and C are qualitatively similar to A and not discussed here.) To enable comparison of the PDFs from four radial locations on a single plot, colored lines are used to highlight the shape of the velocity histograms at the different spatial stations. Before plotting, the histograms are normalized by the maximum number of particles within the most populated velocity bin and then Stineman [22] interpolation is used to smooth the histogram, reducing random variations in height between neighboring bins. As with any low-pass filter, this algorithm reduces the normalized histogram height to a value less than one.

The data in Figs. 4 and 5 are acquired downstream of the venturi's trailing edge at $z/D_{te} = 0.88$. Moving radially inward, the evolution of the velocity PDFs follows the above phenomenological description. Figure 4 depicts the PDF evolution as the probe volume is translated from $r/D_{te} = -0.504$ to -0.450. Similarly, the profiles in Fig. 5 correspond to the probe volume starting at the other side of the swirler at $r/D_{te} = 0.504$ and moving radially inward to $r/D_{te} = 0.450$. The calculated streamwise skewness of each PDF is listed in the figure's legend. The bimodal structure becomes evident at $r/D_{te} = \pm 0.468$. It is at this location where $S_z \approx 0$, defining the boundary between the primary and secondary streams. As the probe volume moves farther away from this location into either the primary or secondary freestreams, the velocity PDFs become more monomodal with the skewness magnitude increasing due to the imbalance in peak heights.

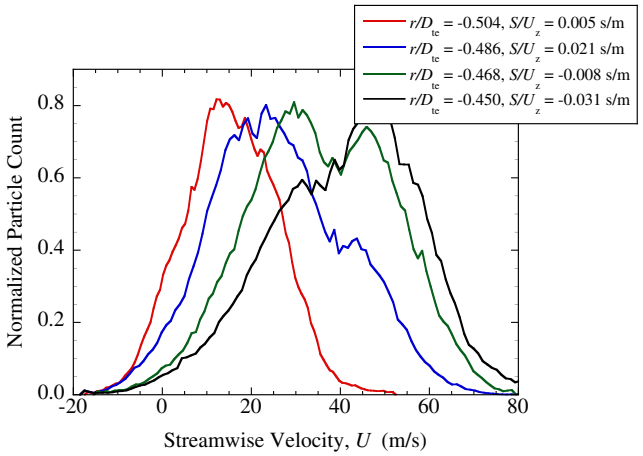

Fig. 4 Swirler A: velocity PDFs across upper transition region between primary and secondary streams.

Another way to view these data is to plot the streamwise skewness for swirlers A, B, and C as shown in Fig. 6. Two pairs of vertical reference lines are used to identify the radial boundaries of the PDF data presented in the previous two figures. Selecting the leftmost reference line and moving radially inward in Fig. 6, the skewness rises from a near zero value in the secondary freestream to a maximum as fluid from the primary stream is encountered. The skewness profile crosses zero when the contribution from both flows becomes equal. It is at this *zero crossing* that the boundary $r/D_{te} = \pm 0.468$ between the two streams is located. Continuing radially inward, the skewness drops quickly below zero as the primary stream begins to dominate the velocity PDF. The near discontinuous drop in the skewness is ideal for identifying the primary–secondary boundaries for an ensemble of swirl cups. Not surprisingly, the zero crossing is nearly identical for the three swirl cups studied here as these components were manufactured with the same tool and finishing processes.

Using this technique, Fig. 7 displays the calculated primary mass flow split (PMFS) versus normalized effective area for three different swirler designs. For reference purposes, the effective area data on the abscissa is normalized by the average effective area for design 1. PMFS represents the fraction of total airflow passing through the primary vanes and is defined as follows:

$$\text{PMFS} = \frac{m_P}{m_T} = \frac{\int_0^{\text{split}} U_z(r) r \mathrm{d}r}{\int_0^{D_{te}/2} U_z(r) r \mathrm{d}r} \tag{3}$$

The upper integration limit in the numerator is determined by the primary–secondary stream boundary where the streamwise skewness crosses zero, that is, $r/D_{te} = \pm 0.468$ in Fig. 6. Table 3 provides the manufacturing details for the seven swirler ensembles plotted in

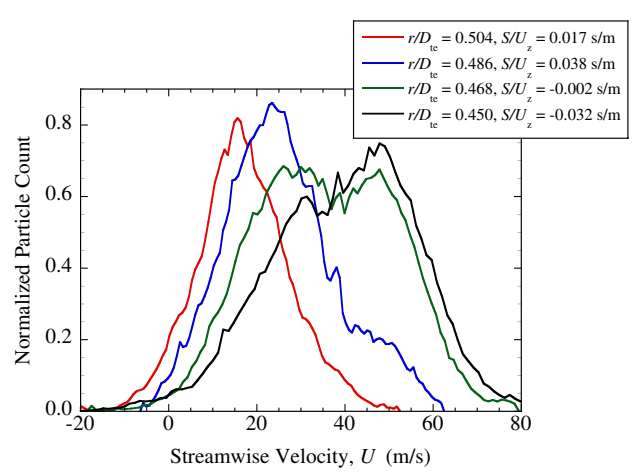

Fig. 5 Swirler A: velocity PDFs across upper transition region between primary and secondary streams.

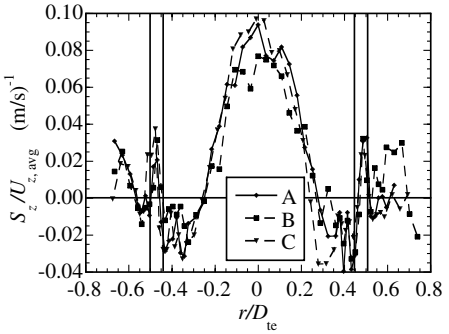

Fig. 6 Mean streamwise skewness profiles acquired at $z/D_{\mathrm{te}} = 0.88$.

the figure. Each ensemble embodies a different design, swirler vendor, and/or finishing method. At least four sets of LDV data (traverses) were acquired for every swirler in each ensemble with the average PMFS values plotted in Fig. 7.

The addition of the PMFS data to Fig. 7 enhances the effective area data, providing a second criterion to judge the swirlers' performance. As expected, the effective area measurements group the three designs into discrete regions. Design 3 swirlers have nearly identical effective areas, yet the maximum PMFS is 50% greater than the minimum. With regards to fuel/air ratios during engine operation, the swirler with the higher PMFS will lean the CTRZ with excess air, potentially extinguishing the local flame. Design 1 swirlers are fairly consistent in both effective area and PMFS. One would expect the performance of these swirlers to be nearly identical since they were not reworked by hand. The variation in design 2 (ensembles 2–6) is attributed to alternate tools and rework processes used to manufacture and finish, respectively, the swirlers. The spread in effective areas is less than their variation in PMFS. The added LDV data suggest that swirlers manufactured with an old tool (ensemble 3) could not be distinguished from those created with a new tool if only A_e measurements were acquired. Instead, the PMFS of ensembles 3 and 6 show that the old tool and new tool are in fact different. In like manner, the average PMFS for ensemble 3 is 30% greater than those that have been abrasively reworked (ensemble 2). Similar analyses to Fig. 7 may be performed using the S_N, TKE, or like metric from the LDV data to compliment the A_e measurements for each swirler.

Streamwise skewness has been employed by other researchers for defining the boundaries between interacting streams. In a related gas turbine combustor study, McGuirk and Palma [11] use skewness and flatness to identify the region within a model combustor where the primary jets (equally spaced around the circumference of the combustor liner) begin to interact with the streamwise flow within the

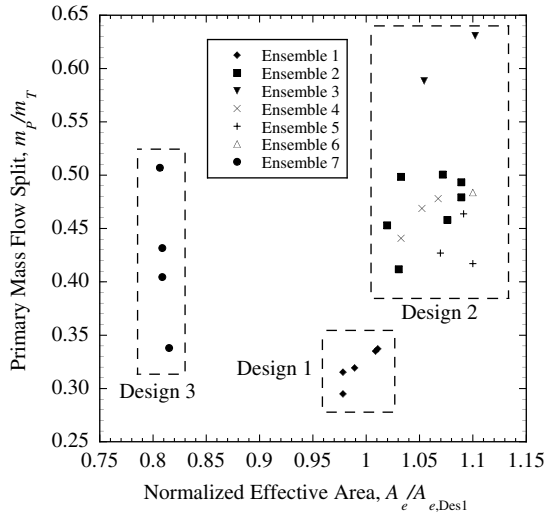

Fig. 7 Swirler performance variation due design and manufacturing methods; see Table 3 for a description of each ensemble.

Table 3 Swirler information

Ensemble	Swirler design	No. swirlers	Vendor	Modification
1	1	5	1	None
2	2	7	2	Abrasive rework
3	2	2	2	Old tool
4	2	3	2	None
5	2	3	2	Vane repair
6	2	1	2	New tool
7	3	4	1	None

liner. Similar to our observations, the bimodality of the velocity histograms was greatest at the near-field intersection between the two streams. At stations further downstream, the skewness values decreased, indicating an increase in turbulent mixing. In our effort, at axial stations greater than $z/D_{\mathrm{te}} > 0.88$, the S_z gradient decreased near the zero crossing ($r/D_{\mathrm{te}} \approx \pm 0.468$), often alternating between positive and negative values.

To complete the discussion of the LDV measurements, the azimuthal skewness profiles are provided in Fig. 8. Comparing Figs. 6 and 8, it is clear that the azimuthal skewness does not embody a sharp gradient near the $r/D_{\mathrm{te}} = \pm 0.468$ boundary. Moreover, the agreement between the three curves in Fig. 8 is not as good as those found in Fig. 6. Unlike the streamwise velocity histograms presented in Figs. 4 and 5, the azimuthal velocity PDFs (not shown) maintain a self-similar shape at the aforementioned radial stations. Distinct changes in modality were not readily observed.

DPIV Results

Although rich in detail, the above LDV measurements present a pointwise statistical view of the local flowfield. The transport of large-scale vortices within the flow is not perceptible in the data. Likewise, Syred and Beér [16] correctly found that the CTRZ is not spatially or temporally stationary. At swirl numbers higher than $S_N > 0.5$, the core systematically rotates about the centerline axis with time at a frequency that is proportional to $f = Q/D_{\mathrm{sh}}^3$, where Q is the volumetric flow rate of air passing through the swirler. Vortices are shed from the nozzle as the CTRZ moves about the swirler centerline. DPIV is used here to observe the position of the CTRZ at different points in time; both side- ($U_z - U_r$) and end-view ($U_r - U_\theta$) mean and instantaneous velocity fields are presented.

To acquire the $U_z - U_r$ velocity plane, the laser sheet is positioned parallel to the centerline of the swirler. The sheet illuminates particulate from downstream of the trailing edge to approximately $z/D_{\mathrm{te}} = 2.1$, past the trailing edge of the quartz shroud. The ensemble-averaged $U_z - U_r$ velocity vector field created from 200 image pairs is presented in Fig. 9. The normalized velocity magnitude $U/\bar{U}_z$ is the plotted variable. Midway along the ordinate axis, a white rectangular mask spans the trailing edge of the cylinder where light-piping effects within the quartz tube caused the CCD pixels to saturate. The DPIV image shows a teardrop shaped recirculation zone centered about the swirler centerline. This flowfield is qualitatively similar to the mean flowfield for $S_N = 0.64$ predicted by Gupta et al. [5]. As shown in the mean streamwise LDV

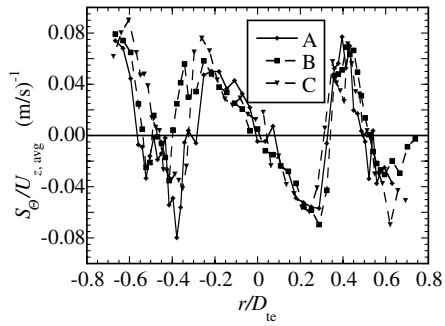

Fig. 8 Mean azimuthal skewness profiles acquired at $z/D_{\mathrm{te}} = 0.88$.

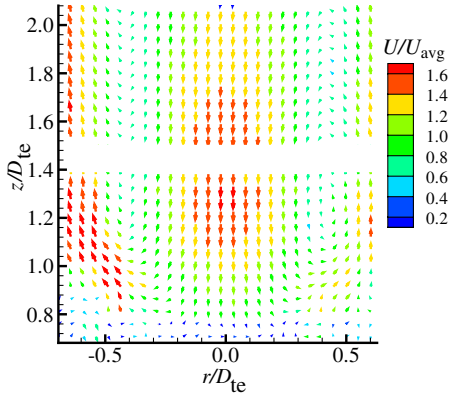

Fig. 9 Ensemble-averaged $U_z - U_r$ vector plot.

measurements in Fig. 2, the forward stagnation point in the toroidal recirculation region lies upstream of the venturi trailing edge. Equally important, the recirculation zone extends well downstream of the region confined by the quartz tube.

Three instantaneous velocity images are displayed in Fig. 10. As expected for this turbulent flowfield, the instantaneous images exhibit large velocity deviations from the ensemble-averaged profile of Fig. 9. Large-scale vortices, highlighted with black circles, are evident downstream of the venturi in the secondary stream. Not surprisingly, the recirculation region remains attached to the venturi trailing edge. In a number of images, parcels of high-velocity streamwise-oriented fluid parcels are evident at the ID of the quartz cylinder. It is unclear whether these streaks originate from the primary or secondary freestreams.

The radial position of the recirculation zone changes dramatically in each instantaneous image, shearing, tilting, and translating from one size of the shroud to the other. This periodic "wagging" of the recirculation zone is reminiscent of a precessing vortex core (PVC) [5,8,12]. However, Roux et al. [9] shows that for true PVC where the core rotates at a single frequency, the azimuthal rms should reach a maximum at $r/D_{te} = 0$. Counter to this, the azimuthal rms profile in Fig. 3b exhibits a local minimum along the swirler centerline. Likewise, Anacleto et al. [12] experimentally verified that PVC begins when $S_N > 0.5$, growing more prominent as the swirl number is increased. The LDV data and images in Fig. 10 suggest that the flow has not yet reached an orderly PVC state.

To gain further insight into the variation of the azimuthal velocity within the primary and secondary regions, end-view DPIV images are acquired. In this configuration, the laser light sheet is oriented normal to the swirler centerline at a streamwise station of $z/D_{te} = 0.88$. The sheet propagates normal to the centerline axis of the swirler, illuminating the particulate contained within the quartz shroud. The CCD camera, positioned at a shallow angle to the swirler centerline, is focused upstream on the z/D_{te} exit plane. Mie scattering from seed particles illuminates the trailing edge of the venturi. As with the side images, the internal reflections of the laser light sheet within the quartz cylinder overwhelm the light scattering from nearby particulate. Care was taken during the processing of the DPIV images to prevent the illuminated quartz cylinder from altering the nearby particle pairs. Unfortunately, the nonphysical blue vectors at the periphery in Fig. 11 are instigated by the interaction of the FFT cross-correlation window with the quartz cylinder.

In the ensemble-averaged velocity image of Fig. 11, an annulus of low velocity fluid separates the primary–secondary stream boundary ($r/D_{te} \approx 0.46$). Again, the average streamwise velocity of this vector field, $\bar{U}_z$, is used to normalize the velocity scale in Figs. 11 and 12. Light reflection from the base region of the venturi trailing edge increases the background noise level, subsequently decreasing the signal-to-noise ratio of the particle pairs in this region. To minimize these reflections, the trailing edge of the venturi was painted black.

Figure 11 shows that the counterclockwise orientation of the velocity vectors across the swirl cup exit is consistent with the azimuthal mean velocity profile in Fig. 2. Equally important, the

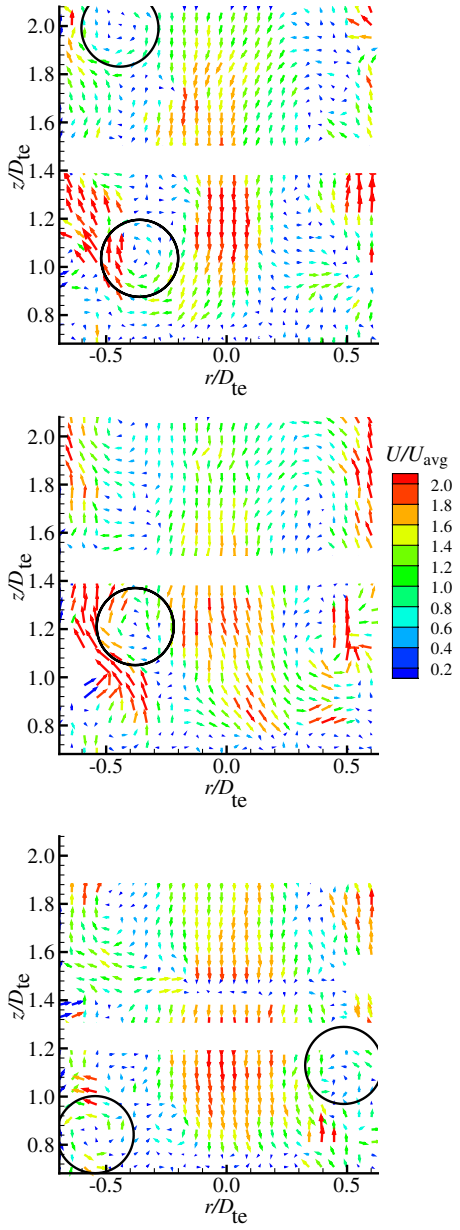

Fig. 10 Instantaneous $U_z - U_r$ vector plots. The trailing edge of the venturi is located at $z/D_{te} = 0.81$.

azimuthal velocity increases with radial distance, similar to solid-body rotation. Higher velocities, upward of $U/\bar{U}_z = 1.9$, are encountered in the secondary stream. In Fig. 11, the peak velocities are biased towards the right-hand side of the image. One possible explanation for this inconsistency is that the DPIV laser light sheet diverges slightly as it travels across the swirler face. While this divergence was minimized at the outset of the experiments, the index of refraction changes as the laser travels through the quartz shroud, emphasizing any divergence in the light sheet. Particles within the thin region of the sheet would move out of the illuminated plane before the CCD camera captures their position in the second DPIV image.

Figure 12 presents three instantaneous end-view images. As expected, the core of the flowfield is not centered, moving from one sector of the quartz shroud to another between images. The bulk movement of this zone is similar to the end-view images of Anacleto et al. [12], where the authors found through smoke visualization that the vortex core formed a "sickle" or crescent shaped recirculation zone. The region outside of the crescent contained flow with positive axial velocities. Because of the limited repetition rate of the DPIV laser (15 Hz) and ambiguity of the primary and secondary stream

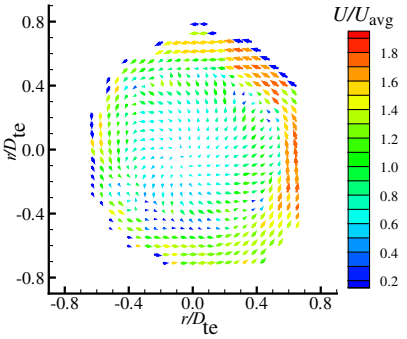

Fig. 11 Ensemble-averaged $U_r - U_\theta$ velocity image collected at $z/D_{te} = 0.88$.

boundaries in Fig. 12, the repetitive paths of the CTRZ cannot be resolved. Syred and Beér [16] note that under reacting conditions, the diffusion flame stationed within the shroud damps the CTRZ motion. Hence, making further inferences regarding swirler performance at flight conditions from the CTRZ shape in isothermal DPIV images could be misleading.

Efforts to correlate the DPIV and LDV velocity profiles were met with limited success. The scattering of laser light off of the venturi trailing edge limited the valid velocity data at $z/D_{te} = 0.88$. However, the $U_z/\bar{U}_z$ velocity profiles (not shown) were qualitatively similar in shape. Higher statistical moments deduced from the DPIV

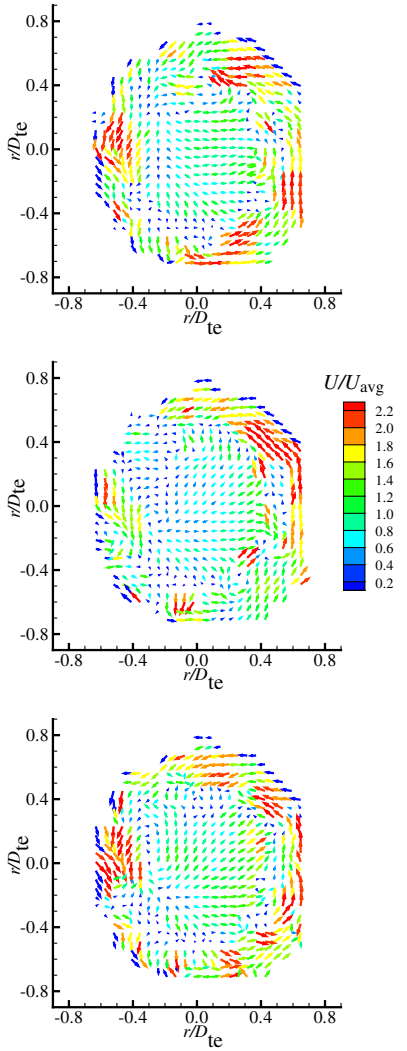

Fig. 12 Instantaneous $U_r - U_\theta$ velocity images collected at $z/D_{te} = 0.88$.

data embodied large uncertainties due to the limited ensemble size of 200 image pairs. Iyer and Woodmansee [21] show that the variance of the skewness decreases with $\sqrt{N}$, favoring LDV over DPIV for analyzing production swirlers. It can be concluded from these data that instantaneous DPIV images capture the time resolved position of the CTRZ. However, using these data to contrast and compare the isothermal behavior of different swirlers is difficult without acquiring an inordinate number of images to ensure a limited uncertainty in the skewness statistic.

Summary and Conclusions

In this article, we have presented a new way to analyze production combustor swirl cups in an isothermal environment using LDV. The zero crossing in the streamwise skewness profile at the trailing edge of the venturi demarcates the interfacial boundary between the primary and secondary streams. As the LDV probe volume is translated from the secondary stream to the primary stream (radially inwards), the streamwise skewness moves from a positive to a negative value in a sharp, nearly discontinuous manner. The velocity PDFs presented here confirm this transition from monomodal profiles at low velocity ($S_z > 0$) to bimodal profiles at the boundary between primary and secondary streams ($S_z = 0$), and then back to monomodal profiles ($S_z < 0$) within the primary stream. While the zero-crossing points for the three swirlers A, B, and C examined were identical, swirlers manufactured with other tool and dies, by different vendors, and/or with alternative finishing methods did not share the same skewness crossing at the trailing edge of the venturi, exhibiting a variation in PMFS.

To employ the skewness analysis technique, a solid a priori understanding of the swirler geometry and approximate bulk velocities of the streams under study are required to identify the correct zero crossing in the streamwise skewness profile. The sensitivity of this parameter to the modalities of the streamwise velocity distribution often adds multiple crossings to the S_z profile. As a redundant check, visualization media, such as TiO_2 particulate, may be added to one of the two coflowing streams to affirm the approximate location of the primary–secondary stream boundary as determined by LDV.

Definition of this fluid boundary is important because downstream of this streamwise station the primary and secondary streams become rapidly intertwined as shown in the instantaneous DPIV data. However, the LDV data at this station can be used to characterize other parameters such as primary mass flow split and swirl number before turbulence within the shear layer convolves the two streams. For instance, in this particular swirler design, the swirl number of the primary stream was approximately 0.55. Yet, the secondary stream had a swirl number of approximately 3 times the primary stream, well above the CTRZ threshold. Therefore, while little or no fluid had been exchanged between the two streams at the venturi trailing edge, the strong swirl in the secondary stream still energized a central toroidal recirculation zone along the swirler centerline by providing a rotating boundary for the primary flow.

Gaining supporting statistically based conclusions from the DPIV data were not feasible. While the DPIV technique provides insightful two-dimensional images of the $U_r - U_\theta$ and $U_z - U_r$ velocity fields, the limited ensemble size (200 image pairs) lends a significant uncertainty to the mean, rms, and skewness statistics. The uncertainty of each one of these moments decreases with the square root of the sample size. However, ensuring that a statistically significant number of particles was present in the region of interest (i.e., at the trailing edge of the venturi) would require more than the 2000 realizations employed in the LDV technique. Therefore, use of the DPIV tool for identifying subtle differences between swirlers is not readily viable in an industrial setting.

That being said, these DPIV images elucidate the temporal nature of the flow. More specifically, instantaneous DPIV images show that the vortex core moves in time about the centerline of the swirler. As the CTRZ shifts, the end-view images show that the azimuthal velocity of the flow within the secondary stream increases. Similarly,

in the side-view images, large-scale vortices are evident within the secondary stream. These axially moving vortices enhance the mixing of the primary stream and the secondary stream.

Acknowledgments

The authors wish to acknowledge the technical support of Simon Sanderson and the assistance of Angelo D'Amico and Ronald Capello in conducting the experiments.

References

[1] Wang, H., McDonell, V. G., Sowa, W. A., and Samuelson, S., "Experimental Study of a Model Gas Turbine Combustor Swirl Cup, Part I: Two-Phase Characterization," *Journal of Propulsion and Power*, Vol. 10, No. 4, 1994, pp. 441–445.

[2] Lefebvre, A. H., *Gas Turbine Combustion*, Hemisphere Publishing, New York, 1983.

[3] Turns, S. R., *An Introduction to Combustion: Concepts and Applications*, McGraw–Hill, New York, 1996.

[4] Favaloro, S. C., Nejad, A. S., and Ahmed, S. A., "Experimental and Computational Investigation of Isothermal Swirling Flow in an Axisymmetric Dump Combustor," *Journal of Propulsion and Power*, Vol. 7, No. 3, 1991, pp. 348–356.

[5] Gupta, A. K., Lilley, D. G., and Syred, N., *Swirl Flows, Energy and Engineering Science*, Abacus Press, Kent, U. K., 1984.

[6] Muruganandam, T. M., Nair, S., Scarborough, D., Neumeier, Y., Jagoda, J., Lieuwen, T., Seitzman, J., and Zinn, B. T., "Active Control of Lean Blowout for Turbine Engine Combustors," *Journal of Propulsion and Power*, Vol. 21, No. 5, 2005, pp. 807–814.

[7] Coghe, A., Solero, G., and Scribano, G., "Recirculation Phenomena in a Natural Gas Swirl Combustor," *Experimental Thermal and Fluid Science*, Vol. 28, No. 7, 2004, pp. 709–714.

[8] Grosjean, N., Graftieaux, L., Michard, M., Hübner, W., Tropea, C., and Volkert, J., "Combining LDA and PIV for Turbulence Measurements in Unsteady Swirling Flows," *Measurement Science and Technology*, Vol. 8, No. 12, 1997, pp. 1523–1532.

[9] Roux, S., Lartigue, G., Poinsot, T., Meier, U., and Bérat, C., "Studies of Mean and Unsteady Flow in a Swirled Combustor Using Experiments, Acoustic Analysis, and Large Eddy Simulations," *Combustion and Flame*, Vol. 141, No. 1–2, 2005, pp. 40–54.

[10] McGuirk, J. J., and Palma, J. M. L. M., "Experimental Investigation of the Flow Inside a Water Model of a Gas Turbine Combustor: Part 1—Mean and Turbulent Flowfield," *Journal of Fluids Engineering*, Vol. 117, No. 3, 1995, pp. 450–458.

[11] McGuirk, J. J., and Palma, J. M. L. M., "Experimental Investigation of the Flow Inside a Water Model of a Gas Turbine Combustor: Part 2—Higher Order Moments and Flow Visualization," *Journal of Fluids Engineering*, Vol. 117, No. 3, 1995, pp. 459–467.

[12] Anacleto, P. M., Fernandes, E. C., Heitor, M. V., and Shtork, S. I., "Swirl Flow Structure and Flame Characteristics in a Model Lean Premixed Combustor," *Combustion Science and Technology*, Vol. 175, No. 8, 2003, pp. 1369–1388.

[13] Weigand, P., Meier, W., Duan, X. R., Stricker, W., and Aigner, M., "Investigations of Swirl Flames in a Gas Turbine Model Combustor I. Flow Field, Structures, Temperature, and Species Distributions," *Combustion and Flame*, Vol. 144, No. 1–2, 2006, pp. 205–224.

[14] Meier, W., Duan, X. R., and Weigand, P., "Investigations of Swirl Flames in a Gas Turbine Model Combustor II. Turbulence-Chemistry Interactions," *Combustion and Flame*, Vol. 144, No. 1–2, 2006, pp. 225–236.

[15] Zhengqi, L., Rui, S., Lizhe, C., Zhixin, W., Shaohua, W., and Yukun, Q., "Effect of Primary Air Flow Types on Particle Distributions in the Near Swirl Burner Region," *Fuel*, Vol. 81, No. 6, 2002, pp. 829–835.

[16] Syred, N., and Beér, J. M., "Combustion in Swirling Flows: A Review," *Combustion and Flame*, Vol. 23, No. 2, 1974, pp. 143–201.

[17] Hogg, R. V., and Tanis, E. A., *Probability and Statistical Inference*, Macmillan, New York, 1993.

[18] Mehta, J. M., Shin, H.-W., and Wisler, D. C., "Mean Velocity and Turbulent Flow- Field Characteristics Inside an Advanced Combustor Swirl Cup," AIAA Paper 89-0215, June 1989.

[19] Wang, H., McDonell, V. G., Sowa, W. A., and Samuelson, S., "Experimental Study of a Model Gas Turbine Combustor Swirl Cup, Part II: Droplet Dynamics," *Journal of Propulsion and Power*, Vol. 10, No. 4, 1994, pp. 446–452.

[20] Adrian, R. J., "Laser Velocimetry," *Fluid Mechanics Measurements*, 2nd ed., edited by R. J. Goldstein, Taylor and Francis, Washington, D.C., 1996, pp. 175–299.

[21] Iyer, V., and Woodmansee, M. A., "Uncertainty Analysis of LDV Measurements in a Swirling Flowfield," *AIAA Journal*, Vol. 43, No. 3, 2005, pp. 512–519.

[22] Stineman, R. W., "A Consistently Well Behaved Method of Interpolation," *Creative Computing*, Vol. 6, No. 7, 1980, pp. 54–57.

T. Lieuwen
Associate Editor